

NUCLEAR SHAPE EVOLUTION IN PALLADIUM ISOTOPES

SMRITI THAKUR[†], PANKAJ KUMAR, VIRENDER THAKUR
VIKESH KUMAR, SHASHI K. DHIMAN

Department of Physics, Himachal Pradesh University
Summer-Hill, Shimla-171005, India

(Received May 25, 2021; accepted October 10, 2021)

The phenomena of shape evolution and shape coexistence are studied in even–even $^{86-134}\text{Pd}$ isotopes by employing the relativistic Hartree–Bogoliubov (RHB) model by employing density-dependent point-coupling parameter sets DD-PC1 and DD-PCX with separable pairing interaction. Our findings of binding energies, quadrupole deformation parameter, charge radii, and two-neutron separation energies as a function of neutron number N are compared with available experimental data and various theoretical models. Our theoretical results predict prolate–oblate shape coexistence in ^{108}Pd isotope.

DOI:10.5506/APhysPolB.52.1433

1. Introduction

It is known that nuclei lying near shell closure $Z = 50$ exhibit shape transitions and shape coexistence [1, 2] with the increase in neutron number. Radioactive Ion Beam (RIB) facilities and sensitive detection technologies have opened new possibilities to study the structure and properties of various exotic nuclei. The nuclei in this mass region exhibit a rapid change of nuclear shapes with competing spherical, axially symmetric prolate and oblate, and triaxial shapes, resulting in shape instabilities and coexistence of nuclear shape transitions in isotopic chains [3]. In addition to structural richness, another interesting characteristics of this region is its involvement in the astrophysical rapid neutron capture process (also called r-process), one of the main nucleosynthesis mechanisms which leads to the production of heavy neutron-rich nuclei in the universe [4, 5].

[†] Corresponding author: thakursmriti14@gmail.com

Recent studies [6] prove that $^{112-116}\text{Pd}$ isotopes show shape coexistence. Reference [7] suggests that the shape coexistence should occur in the region of $N = 60$ to 70 , around $Z = 50$. The deformation energy surfaces of $^{114-128}\text{Pd}$ isotopes have also been studied using constrained HF + BCS calculations with the Skyrme force SLy4 [8]. The potential energy curves for $^{96-118}\text{Pd}$ isotopes obtained with the Gogny D1S force are also observed [9]. A systematic study of even-even nuclei ranging from $Z = 10-110$ has been performed in Ref. [10] within the framework of Hartree-Fock-Bogoliubov (HFB) formalism using the Gogny D1S interaction, which includes predicted the values of deformation parameters, beta and gamma, and the shape transition for $^{106-152}\text{Pd}$ isotopes.

In the present work, the quantities of interest are the nuclear potential energy curves, nuclear binding energy, two-neutron separation energies (S_{2n}), the differential variation in two-neutron separation energy (dS_{2n}), the root-mean-square charge distribution (R_c) for the even-even $^{86-134}\text{Pd}$ isotopes. The calculations are performed by taking axial symmetry into account. The covariant density functional theory with density-dependent point-coupling interactions DD-PC1 [11] and DD-PCX [12] are employed with separable pairing interaction [13–15].

The paper is organized as follows. In Section 2, a review of the theoretical formalism used is introduced. Section 3 contains the results obtained for nuclear potential energy curves, nuclear binding energy, two-neutron separation energy (S_{2n}), the differential variation in two-neutron separation energy (dS_{2n}), the root-mean-square charge distribution (R_c), which are compared with the experimental data. Section 4 summarizes the main conclusions.

2. Theoretical framework

The self-consistent mean field models (SCMF) are a powerful tool [16–19] for the investigation of nuclear structure properties, low-energy dynamics over the whole nuclide periodic chart and nuclear matter properties up to dense nuclear matter densities. The SCMF models are mainly based on the effective nuclear energy density functionals approach, and can be constructed as functionals of one-body nucleon density matrices that correspond to the Slater-determinant of the single-particle or single-quasi-particle state. Nuclear SCMF models effectively map the many-body problem onto a one-body problem, and the exact Nuclear Energy Density Functional (NEDF) is approximated by simple, mostly analytical, functionals of powers and gradients of ground-state nucleon densities and currents, representing distributions of matter, spins, momentum, and kinetic energy. For completeness, we briefly describe the Relativistic Nuclear Density Functional (RMF-NDF) employed in the present calculation as below.

2.1. The point-coupling model

The Lagrangian for density-dependent point-coupling models includes the isoscalar–scalar $(\bar{\psi}\psi)^2$, isoscalar–vector $(\bar{\psi}\gamma_\mu\psi)(\bar{\psi}\gamma^\mu\psi)$, and isovector–vector $(\bar{\psi}\vec{\tau}\gamma_\mu\psi)\cdot(\bar{\psi}\vec{\tau}\gamma^\mu\psi)$. Four-fermion contact interactions in the isospace–space can be written as [11]

$$\begin{aligned} \mathcal{L} = & \bar{\psi}(i\boldsymbol{\gamma}\cdot\partial - m)\psi - \frac{1}{2}\alpha_S(\rho)(\bar{\psi}\psi)(\bar{\psi}\psi) \\ & - \frac{1}{2}\alpha_V(\rho)(\bar{\psi}\boldsymbol{\gamma}\boldsymbol{\mu}\psi)(\bar{\psi}\boldsymbol{\gamma}_\boldsymbol{\mu}\psi) - \frac{1}{2}\alpha_{TV}(\rho)(\bar{\psi}\vec{\tau}\boldsymbol{\gamma}\boldsymbol{\mu}\psi)(\bar{\psi}\vec{\tau}\boldsymbol{\gamma}_\boldsymbol{\mu}\psi) \\ & - \frac{1}{2}\delta_S(\partial_\nu\bar{\psi}\psi)(\partial^\nu\bar{\psi}\psi) - e\bar{\psi}\boldsymbol{\gamma}\cdot A\frac{1-\tau_3}{2}\psi. \end{aligned} \quad (1)$$

The above Lagrangian density is consisting of the free-nucleon Lagrangian, the point-coupling interaction terms, the coupling of the protons to the electromagnetic field, and a derivative term accounts for leading effects of finite-range interactions. The derivative term in Eq. (1) is crucial for a quantitative description of nuclear density distribution, for example, nuclear radii. Similar interactions can be included in each space–isospace channel, but in practice, data only constrain a single derivative term, for instance, $\delta_S(\partial_\nu\bar{\psi}\psi)(\partial^\nu\bar{\psi}\psi)$. The point-coupling Lagrangian, Eq. (1), does not include isovector–scalar terms. In the meson-exchange picture, this channel is represented by the exchange of an effective δ meson, and its inclusion introduces a proton–neutron effective mass splitting and enhances the isovector spin–orbit potential. Although the spin–orbit strength has a relatively well-defined value, the distribution between the scalar and vector channels is not determined by ground-state data.

From the Lagrangian density in Eq. (1), one can calculate the Hamiltonian density $\mathcal{H}(\mathbf{r})$ and hence the energy density functional for the point-coupling model as

$$\begin{aligned} \mathcal{E}_{\text{RMF}}[\psi, \bar{\psi}, A_\mu] = & \int d^3r \mathcal{H}(\mathbf{r}) = \sum_{i=1}^A \int d^3r \psi_i^\dagger (\alpha p + \beta m) \psi_i \\ & - \frac{1}{2}(\nabla A)^2 + \frac{1}{2}e \int d^3r j_p^\mu A_\mu \\ & + \frac{1}{2} \int d^3r \left[\alpha_S \rho_s^2 + \alpha_V j_\mu j^\mu + \alpha_{TV} \vec{j}_\mu \cdot \vec{j}^\mu + \delta_S \rho_s \square \rho_s \right]. \end{aligned} \quad (2)$$

The functional form of the point-couplings chosen is

$$\alpha_i(\rho) = a_i + (b_i + c_i x) e^{-d_i x}, \quad (i = S, V, TV), \quad (3)$$

where $x = \rho/\rho_{\text{sat}}$ and $\rho_{\text{sat}} (= 0.152 \text{ fm}^{-3})$ denotes the nucleon density in symmetric nuclear matter at saturation point, and Eq. (3) is used to adjust the model parameters. In Table I, we present the parameters of recently developed density-dependent point-coupling interactions DD-PC1 [11] and DD-PCX [12].

TABLE I

The parameters of density-dependent point coupling DD-PC1 [11] and DD-PCX [12] interactions in the Lagrangian. The value of saturation density is set to 0.152 fm^{-3} .

Parameter	DD-PC1	Parameter	DD-PCX	Units
m	939	m	939	MeV
a_S	-10.0462	a_S	-10.979243836	fm^2
b_S	-9.1504	b_S	-9.038250910	fm^2
c_S	-6.4273	c_S	-5.313008820	fm^2
d_S	1.3724	d_S	1.379087070	
a_V	5.9195	a_V	6.430144908	fm^2
b_V	8.8637	b_V	8.870626019	fm^2
d_V	0.6584	d_V	0.655310525	
b_{TV}	1.8360	b_{TV}	2.963206854	fm^2
d_{TV}	0.6403	d_{TV}	1.309801417	
δ_S	-0.8149	δ_S	-0.878850922	fm^4
G	-728	G_n	-800.663126037	MeV fm^3
		G_p	-773.776776597	MeV fm^3

2.2. Relativistic Hartree–Bogoliubov approximation with a separable pairing interaction

The relativistic Hartree–Bogoliubov model [16, 17] provides a unified description of particle–particle (pp) and particle–hole (ph) correlations on SCMF level by using the averages of two potentials: self-consistent mean-field potential that encloses the long-range ph correlations and a pairing field potential which sums up the pp correlations. In the RHB model, in the presence of pairing, density matrix can be generalized in two densities, the normal density $\hat{\rho}$, and pairing tensor $\hat{\kappa}$. The relativistic Hartree–Bogoliubov energy density functional can be written as [14]

$$E_{\text{RHB}}[\hat{\rho}, \hat{\kappa}] = E_{\text{RMF}}[\hat{\rho}] + E_{\text{pair}}[\hat{\kappa}], \quad (4)$$

where $E_{\text{RMF}}[\hat{\rho}]$ is the nuclear energy density functional for point coupling models given in Eq. (2).

The pairing part of RHB functional is given by

$$E_{\text{pair}}[\hat{\kappa}] = \frac{1}{4} \sum_{n_1 n'_1} \sum_{n_2 n'_2} \kappa_{n_1 n'_1}^* \langle n_1 n'_1 | V^{PP} | n_2 n'_2 \rangle \kappa_{n_2 n'_2}, \quad (5)$$

where $\langle n_1 n'_1 | V^{PP} | n_2 n'_2 \rangle$ denote the matrix elements of the two-body pairing interaction and indices n_1, n'_1, n_2 , and n'_2 denote quantum numbers that specify the Dirac indices of the spinor. The pairing field Δ reads

$$\Delta_{n_1 n'_1} = \frac{1}{2} \sum_{n_2 n'_2} \langle n_1 n'_1 | V^{PP} | n_2 n'_2 \rangle \kappa_{n_2 n'_2}. \quad (6)$$

The two-body interaction matrix elements of the pairing field Δ have been computed by using a separable form of the Gogny force introduced for hybrid RHB calculations [20] for spherical and deformed nuclei [21]. The pairing force is separable in momentum space and can be transformed from momentum to coordinate space

$$V^{PP}(\mathbf{r}_1, \mathbf{r}_2, \mathbf{r}'_1, \mathbf{r}'_2) = -G \delta(\mathbf{R} - \mathbf{R}') P(\mathbf{r}) P(\mathbf{r}'), \quad (7)$$

where $\mathbf{R} = \frac{1}{\sqrt{2}}(\mathbf{r}_1 + \mathbf{r}_2)$ and $\mathbf{r} = \frac{1}{\sqrt{2}}(\mathbf{r}_1 - \mathbf{r}_2)$ represent the center of mass and the relative coordinates, respectively, and $P(\mathbf{r})$ is written as

$$P(\mathbf{r}) = \frac{1}{(4\pi a^2)^{3/2}} e^{-r^2/2a^2}. \quad (8)$$

The two parameters G (pairing interaction parameter) and a (pairing width = 0.644 fm) have been adjusted to reproduce the density dependence of the gap at the Fermi surface. It is calculated with the D1S Gogny force [13, 14, 19, 22]. The pairing force has a finite range and by virtue of the presence of the factor $\delta(\mathbf{R} - \mathbf{R}')$, it also conserves translational invariance. Even though this force is not completely separable in the coordinate space, the anti-symmetrized pp matrix elements can be expressed as a sum of a finite number of separable terms in the harmonic oscillator basis

$$\langle n_1 n_2 | V^{PP} | n'_1 n'_2 \rangle_a = \sum_N W_{n_1 n_2}^{N*} W_{n'_1 n'_2}^N. \quad (9)$$

Now, the pairing field Δ becomes, $\Delta_{n_1 n_2} = \sum_N P_N W_{n_1 n_2}^{N*}$ with $P_N = \frac{1}{2} \text{Tr}(W^N \kappa)$, subsequently, the pairing energy in the nuclear ground state is given as [21]

$$E_{\text{pair}} = -G \sum_N P_N^* P_N. \quad (10)$$

The pairing correlations have been treated in the BCS constant gap approximation along with the empirical pairing gaps, because the pairing correlations contribute much less to the total binding energies of a nucleus.

3. Results and discussion

A reliable convergence in mean-field formalism can be achieved by taking a large number of oscillator shells. However, the computational time increases drastically with an increase in number of oscillator shells. This problem can be resolved by limiting the number of shells and studying the convergence behavior. In the present work, we have done a convergence study of $N = 60$ and $N = 70$ isotopes of Pd. Figure 1 displays the results of binding energy, charge radius (R_c), and quadrupole deformation parameter (β_2) as a function of the number of oscillator shells. The variation in the results ranges around 0.1% for binding energy, 0.02% for charge radius, and around 1% for quadrupole deformation parameter in the case of ^{106}Pd . The variation in the results of binding energy is around 0.05%, 0.04% for charge radius, and 1–2% for quadrupole deformation parameter in the case of ^{116}Pd . All the above variations are calculated on an increasing number of oscillator shells from 12 to 20. Therefore, we have used 12 major oscillator shells to save the computation time and obtained reasonably converging mean-field solutions.

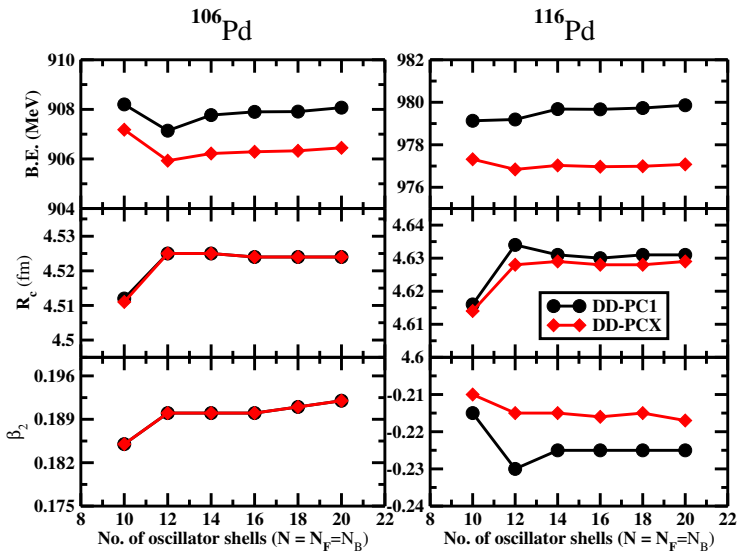


Fig. 1. (Color online) The results of convergence study of the binding energy, charge radii (R_c), and quadrupole deformation parameter (β_2) for ^{106}Pd and ^{116}Pd nuclei, with DD-PC1 and DD-PCX parameter sets, as a function of oscillator shells ($N = N_F = N_B$).

3.1. Potential energy curves

Potential energy curves obtained from the self-consistent relativistic mean-field theory play a very eminent role in determining of the ground state of a nuclei similar to the non-relativistic calculations [23]. The quadrupole deformation is most dominant, hence other deformation coordinates are neglected in the present study for low computation time, cost, and simplicity.

In Figs. 2–4, the results obtained by preserving axial symmetry are presented in the form of multipanel plots of the potential energy curves as a function of quadrupole deformation parameter β_2 for even–even $^{86-134}\text{Pd}$ isotopes and we observe the shape transitions in each system with an increase in neutron number N . We observe that the ^{86}Pd with $N = 40$ has a spherical shape and as we move away from sub-shell closure at $N = 40$, the evolution of deformed shapes is noticed. A prolate shape is observed in $^{88-94}\text{Pd}$ and as we move towards the shell closure $N = 50$ in ^{96}Pd , a spherical shape is regained. Moving away from shell closure $N = 50$, we observe the energy curve with the minimum energy exhibiting prolate deformation. In ^{108}Pd , we observe two minima, the primary minimum with $\beta_2 = 0.20$ corresponding to the prolate shape and the secondary energy minimum with $\beta_2 = -0.24$ corresponding to the oblate shape. We then observe a transition in $^{110-118}\text{Pd}$ isotopes with the minimum energy corresponding to oblate

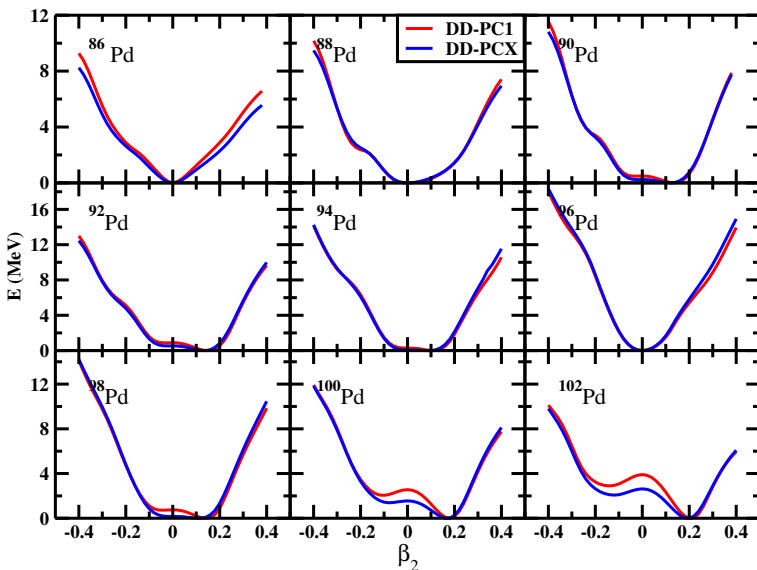


Fig. 2. (Color online) The potential energy curves, calculated with DD-PC1 and DD-PCX interactions, as a function of quadrupole deformation parameter β_2 for $^{86-102}\text{Pd}$ isotopes. The energies are normalized with respect to the binding energy of the global minima.

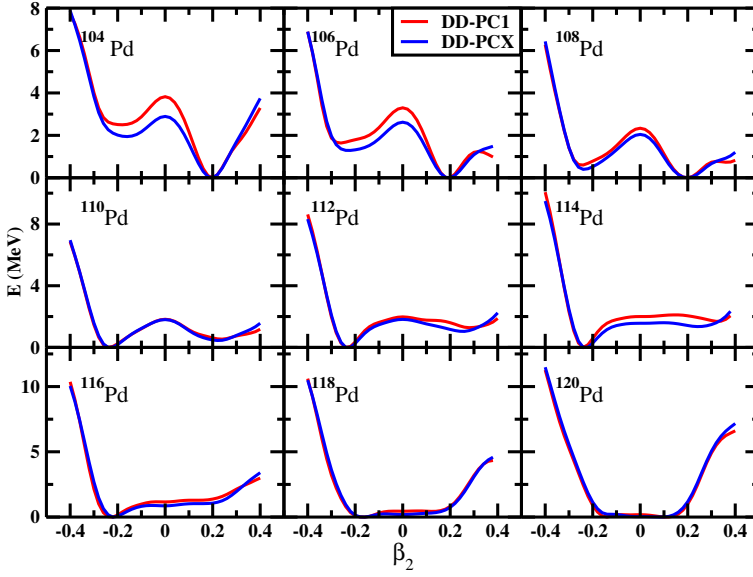


Fig. 3. (Color online) The same as Fig. 2, for $^{104-120}\text{Pd}$ isotopes.

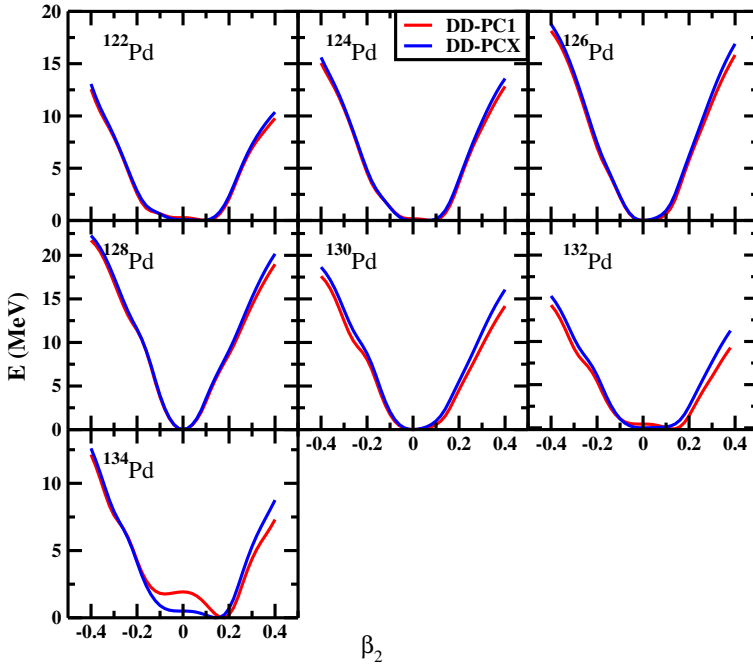


Fig. 4. (Color online) The same as Fig. 2, for $^{122-134}\text{Pd}$ isotopes.

shapes. An oblate-to-prolate shape transition is observed in $^{122-124}\text{Pd}$ and then the spherical shape is achieved as we move towards $N = 82$ shell closure in ^{128}Pd . After $N = 84$, again a prolate shape is regained in $^{132-134}\text{Pd}$. Our results for shape evolution are in accordance with the FRDM calculations [24].

3.2. Nuclear binding energy

The nuclear binding energy is one of the most crucial characteristics not only in nuclear physics but also in other fields, such as astrophysics [25, 26]. We present the detailed values of binding energies and quadrupole deformations in Table II. The results calculated with the DD-PC1 and

TABLE II

The binding energy E (in MeV) and the quadrupole deformation parameter β_2 for the ground states and few selective first intrinsic excited states of $^{86-134}\text{Pd}$ isotopes compared with NL3 [6] and with available experimental data [27, 28].

Nuclei	DD-PC1		DD-PCX		NL3 [6]		[27, 28]	
	B.E.	β_2	B.E.	β_2	B.E.	β_2	B.E.	β_2
^{86}Pd	665.06	0.0	662.78	0.0	—	—	—	—
^{88}Pd	697.35	0.0	695.97	0.0	697.8	0.002	—	—
^{90}Pd	728.89	0.14	727.81	0.12	730.0	0.094	729.12	—
^{92}Pd	759.38	0.14	758.55	0.14	760.9	0.101	759.04	—
^{94}Pd	788.01	0.10	787.54	0.10	789.5	0.004	788.04	—
^{96}Pd	816.12	0.0	815.95	0.0	817.4	0.001	816.30	—
^{98}Pd	835.13	0.14	834.72	0.10	836.9	0.003	834.93	—
^{100}Pd	854.82	0.18	854.08	0.16	855.9	0.136	852.91	—
^{102}Pd	873.71	0.20	872.59	0.20	874.2	0.176	870.33	0.196
^{104}Pd	890.83	0.20	889.77	0.20	891.1	0.189	887.26	0.209
^{106}Pd	907.12	0.20	905.92	0.20	906.9	0.187	903.75	0.229
^{108}Pd	922.51	0.20	921.25	0.20	921.8	0.190	919.80	0.243
	921.91	-0.24	920.85	-0.24	—	—	—	—
^{110}Pd	937.74	-0.24	936.31	-0.24	936.1	0.240	935.35	0.257
^{112}Pd	952.78	-0.24	950.93	-0.24	951.8	-0.231	950.27	0.220
^{114}Pd	966.81	-0.24	964.51	-0.24	965.7	-0.23	964.49	0.164
^{116}Pd	979.18	-0.22	976.84	-0.22	977.9	-0.221	977.97	0.207
^{118}Pd	991.025	-0.16	988.48	-0.16	989.1	-0.198	990.56	—
^{120}Pd	1002.78	-0.14	1000.02	0.08	1000.6	-0.163	1002.33	—
	1002.77	0.12	—	—	—	—	—	—
^{122}Pd	1014.45	0.10	1011.28	0.08	1011.9	0.115	1013.47	—
^{124}Pd	1025.53	0.08	1021.95	0.06	1022.8	0.104	1024.09	—
^{126}Pd	1036.20	0.0	1032.29	0.0	1032.4	0.073	1034.29	—
^{128}Pd	1046.69	0.0	1042.25	0.0	1041.5	0.001	1044.12	—
^{130}Pd	1048.90	0.0	1044.49	0.0	1044.5	0.027	1047.93	—
^{132}Pd	1051.51	0.12	1046.40	0.0	1048.7	0.130	1051.56	—
^{134}Pd	1054.79	0.18	1048.51	0.14	—	—	1055.04	—

DD-PCX interactions are compared with the theoretical results obtained by NL3 interactions [6], PC-PK1 [27], and experimental results [28]. Our findings are also comparable to the theoretical results obtained by NL3* interactions [6], D1S-Gogny interactions [10], and the experimental data in Ref. [29].

In Fig. 5, the variation of quadrupole deformation parameter β_2 with an increase in neutron number N is presented and compared with the finite-range droplet model (FRDM) calculations [24] and with the available experimental data [28]. The experimental values of β_2 are extracted from the experimental $B(E2)\uparrow$ values using the Bohr model of nuclear deformation [30]. We observe an interesting shape transition as moving forward from $N = 50$ shell closure. A prolate deformation develops in $N = 52$ to $N = 60$ with β_2 ranging from 0.1–0.2. We observed the shape transition from prolate to oblate and then oblate to prolate in Fig. 5, and these deformed configurations again become spherical as approaching towards the shell closure at $N = 82$. A reasonable agreement is seen between the experimental data and theoretically calculated values of the quadrupole deformation parameter (β_2).

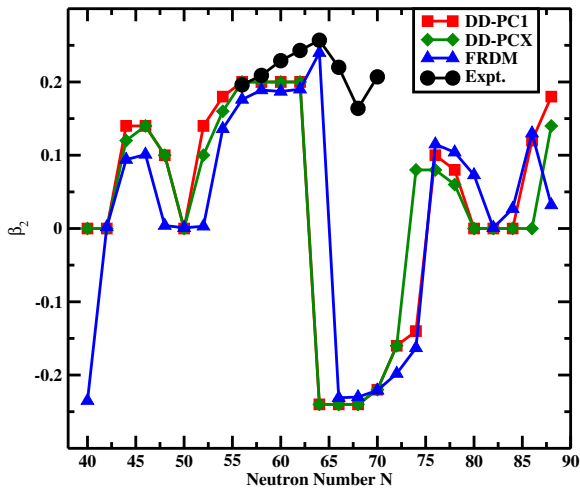


Fig. 5. (Color online) The variation of quadrupole deformation parameter β_2 with respect to neutron number N . The results are compared with the FRDM calculations [24] and experimental data [28].

3.3. Two-neutron separation energy

The two-neutron separation energy S_{2n} can be calculated using the ground-state nuclear binding energies using relation

$$S_{2n}(Z, N) = \text{B.E.}(Z, N) - \text{B.E.}(Z, N - 2). \quad (11)$$

It gives information about the stability of a nucleus against the emission of two neutrons and hence defines the neutron drip lines. The systematics of two-neutron separation energy S_{2n} for $^{86-134}\text{Pd}$ isotopes are presented in Fig. 6. It is observed that two-neutron separation energy decreases smoothly with the increase in number of neutrons, and sharp discontinuities appear at neutron magic numbers at $N = 50$ and 82 due to the presence of neutron shell closures. The theoretical results calculated with DD-PC1 and DD-PCX parameter sets are compared with the theoretical models [6, 10, 27] and available experimental data [29]. In terms of energy, we can say that the energy necessary to remove two neutrons from a magic nucleus is much higher than that to remove two neutrons from the nucleus (Z, N magic+2), which breaks the regular trend.

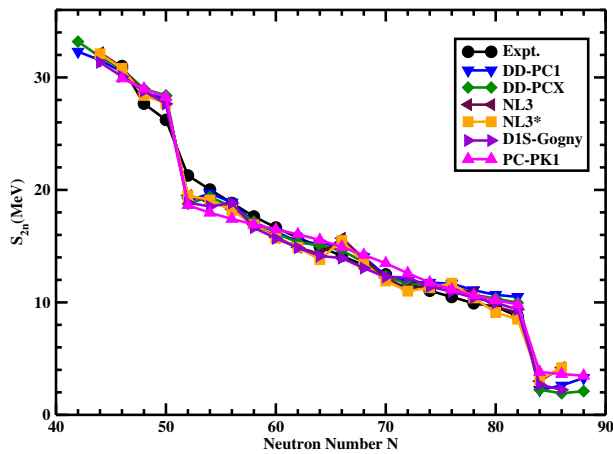


Fig. 6. (Color online) The two-neutron separation energy S_{2n} (in MeV) as a function of neutron number from the DD-PC1 and DD-PCX force parameters are compared with [6, 10, 27] and experimental data [29].

The differential variation of the two-neutron separation energy $dS_{2n}(Z, N)$ with respect to neutron number N is defined as

$$dS_{2n}(Z, N) = \left| \frac{S_{2n}(Z, N + 2) - S_{2n}(Z, N)}{2} \right|. \quad (12)$$

The $dS_{2n}(Z, N)$ investigates the rate of change of separation energy with respect to the neutron number in an isotopic chain. In Fig. 7, we have plotted the results for $dS_{2n}(Z, N)$ calculated using DD-PC1 and DD-PCX interactions and compared them with NL3, NL3* [6], D1S Gogny [10], PC-PK1 [27] interactions, and available experimental data [29]. A sharp rise in the values of $dS_{2n}(Z, N)$ shows the signature of neutron shell closure at $N = 50$ and 82 .

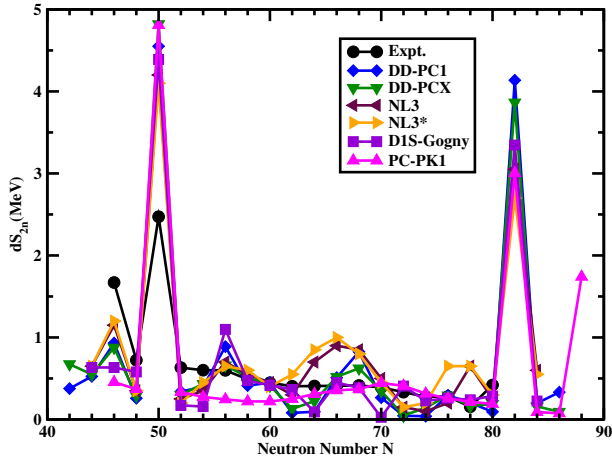


Fig. 7. (Color online) The differential variation in two-neutron separation energy dS_{2n} (in MeV) as a function of neutron number from the DD-PC1 and DD-PCX force parameters are compared with [6, 10, 27] and experimental data [29].

3.4. Root-mean-square charge radius

The nuclear charge radius is one of the most sensitive characteristics to explore the structural evolution in nuclei. In Fig. 8, we present the trend of root-mean-square charge radii R_c [fm] as a function of neutron number N , calculated using CDFT with the DD-PC1 and DD-PCX interactions. The

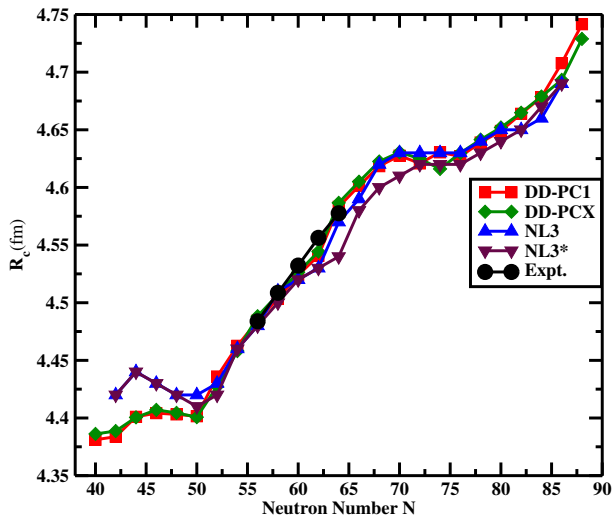


Fig. 8. (Color online) Nuclear charge radii (R_c) as a function of neutron number. The comparison is shown with data in [6, 31].

theoretical results are compared with the available experimental data [31] and theoretical models [6]. We observe a smooth increase in charge radii with an increase in neutron number which shows that the deformation of prolate minima is nearly the same as one moves from $N = 54$ to $N = 62$. The sharp discontinuities in R_c [fm] at $N = 50$ and 82 account for the traditional shell closures. A small change in slope at $N = 64$ and 74 can be related to the sudden shape transition from prolate to oblate and oblate to prolate, respectively. The detailed values of R_c [fm] are presented in Table III. The calculated results with DD-PC1 and DD-PCX interactions are compared with the theoretical results obtained by NL3 and NL3* interactions [6] and PC-PK1 [27].

TABLE III

The root-mean-square charge radius R_c [fm] for the ground states of $^{86-134}\text{Pd}$ nuclei compared with the theoretical models [6, 10] and experimental data [31] wherever available.

Nuclei	DD-PC1	DD-PCX	NL3 [6]	NL3* [6]	D1S Gogny [10]	Experiment [31]
^{86}Pd	4.381	4.386	—	—	—	—
^{88}Pd	4.383	4.389	4.42	4.42	4.37	—
^{90}Pd	4.401	4.401	4.44	4.44	4.37	—
^{92}Pd	4.404	4.407	4.43	4.43	4.38	—
^{94}Pd	4.403	4.404	4.42	4.42	4.38	—
^{96}Pd	4.401	4.401	4.42	4.41	4.38	—
^{98}Pd	4.435	4.427	4.43	4.42	4.40	—
^{100}Pd	4.462	4.458	4.46	4.46	4.45	—
^{102}Pd	4.484	4.488	4.48	4.48	4.46	4.4839
^{104}Pd	4.503	4.507	4.51	4.50	4.48	4.5086
^{106}Pd	4.523	4.526	4.52	4.52	4.50	4.5322
^{108}Pd	4.540	4.544	4.53	4.53	4.52	4.5563
^{110}Pd	4.583	4.586	4.57	4.54	4.53	4.5776
^{112}Pd	4.601	4.605	4.59	4.58	4.56	—
^{114}Pd	4.618	4.622	4.62	4.60	4.57	—
^{116}Pd	4.627	4.631	4.63	4.61	4.59	—
^{118}Pd	4.621	4.625	4.63	4.62	4.59	—
^{120}Pd	4.630	4.616	4.63	4.62	4.59	—
^{122}Pd	4.630	4.630	4.63	4.62	4.60	—
^{124}Pd	4.627	4.642	4.64	4.63	4.62	—
^{126}Pd	4.639	4.652	4.65	4.64	4.63	—
^{128}Pd	4.649	4.665	4.65	4.65	4.64	—
^{130}Pd	4.678	4.679	4.66	4.67	4.65	—
^{132}Pd	4.708	4.693	4.69	4.69	4.66	—
^{134}Pd	4.742	4.729	—	—	4.67	—

4. Conclusion

The present study is done using the relativistic Hartree–Bogoliubov (RHB) model with the density-dependent point-coupling force parameter sets DD-PC1 and DD-PCX, and the pairing correlations are taken into account by employing an interaction that is separable in momentum space. It includes the systematics of binding energy, two-neutron separation energy, the differential variation in two-neutron separation energy, r.m.s. charge radii for the even–even isotopes of $^{86-134}\text{Pd}$. The phenomena of shape evolution and shape coexistence have been observed by taking axial symmetry into account. The value of quadrupole deformation parameter β_2 varies from -0.4 to 0.4 and the number of oscillator shells (number of fermions and number of bosons) are taken to be 12 in our study. In ^{108}Pd isotope, we observe the prolate–oblate shape coexistence with almost degenerate energies. Another oblate–prolate shape coexistence is observed in ^{120}Pd isotope with only the DD-PC1 interaction. Nearly the same deformation of prolate minima from $N = 54$ to $N = 62$ leads to a smooth increase in charge radii with an increase in neutron number. A sudden shape transition from prolate to oblate and oblate to prolate at $N = 64$ and 74 , respectively, results in the small change in slope of R_c . Our theoretical results for the ground-state properties in Pd isotopic mass chain calculated using the density-dependent point-coupling parameter set of DD-PC1 and DD-PCX are in good agreement with the available experimental data and with results obtained from different theoretical models.

The authors would like to thank the Himachal Pradesh University for providing computational facilities and the anonymous referee for a thorough inspection of the manuscript and helpful comments.

REFERENCES

- [1] W. Nazarewicz *et al.*, «Coexistence in even-mass nuclei», *Phys. Rep.* **215**, 101 (1992).
- [2] K. Heyde, J.L. Wood, «Shape coexistence in atomic nuclei», *Rev. Mod. Phys.* **83**, 1467 (2011).
- [3] S. Nishimura, «Beta–gamma spectroscopy at RIBF», *Prog. Theor. Exp. Phys.* **2012**, 03C006 (2012).
- [4] E.M. Burbidge, G.R. Burbidge, W.A. Fowler, F. Hoyle, «Synthesis of the Elements in Stars», *Rev. Mod. Phys.* **29**, 547 (1957).
- [5] J.J. Cowan, F.-K. Thielemann, J.W. Truran, «The r-process and nucleochronology», *Phys. Rep.* **208**, 267 (1991).

- [6] M. Bhuyan, «Structural evolution in transitional nuclei of mass $82 \leq a \leq 132$ », *Phys. Rev. C* **92**, 034323 (2015).
- [7] A. Martinou *et al.*, «Nucleon numbers for nuclei with shape coexistence», *HNPS Adv. Nucl. Phys.* **26**, 96 (2019).
- [8] P. Sarriguren, « β -decay properties of neutron-rich Ge, Se, Kr, Sr, Ru, and Pd isotopes from deformed quasiparticle random-phase approximation», *Phys. Rev. C* **91**, 044304 (2015).
- [9] L.M. Robledo, R.R. Rodríguez-Guzmán, P. Sarriguren, «Evolution of nuclear shapes in medium mass isotopes from a microscopic perspective», *Phys. Rev. C* **78**, 034314 (2008).
- [10] J.P. Delaroche *et al.*, «Structure of even–even nuclei using a mapped collective Hamiltonian and the D1S Gogny interaction», *Phys. Rev. C* **81**, 014303 (2010).
- [11] T. Nikšić, D. Vretenar, P. Ring, «Relativistic nuclear energy density functionals: Adjusting parameters to binding energies», *Phys. Rev. C* **78**, 034318 (2008).
- [12] T. Marketin, E. Yüksel, N. Paar, «Optimizing the relativistic energy density functional with nuclear ground state and collective excitation properties», *Phys. Rev. C* **99**, 034318 (2019).
- [13] Y. Tian, Z.-y. Ma, P. Ring, «Axially deformed relativistic Hartree Bogoliubov theory with a separable pairing force», *Phys. Rev. C* **80**, 024313 (2009).
- [14] Y. Tian, Z.-y. Ma, P. Ring, «A finite range pairing force for density functional theory in superfluid nuclei», *Phys. Lett. B* **676**, 44 (2009).
- [15] T. Nikšić *et al.*, «3D relativistic Hartree–Bogoliubov model with a separable pairing interaction: Triaxial ground-state shapes», *Phys. Rev. C* **81**, 054318 (2010).
- [16] D. Vretenar, A.V. Afanasjev, G.A. Lalazissis, P. Ring, «Relativistic Hartree–Bogoliubov theory: static and dynamic aspects of exotic nuclear structure», *Phys. Rep.* **409**, 101 (2005).
- [17] J. Meng *et al.*, «Relativistic continuum Hartree Bogoliubov theory for ground-state properties of exotic nuclei», *Prog. Part. Nucl. Phys.* **57**, 470 (2006).
- [18] J.R. Stone, P.G. Reinhard, «The Skyrme interaction in finite nuclei and nuclear matter», *Prog. Part. Nucl. Phys.* **58**, 587 (2007).
- [19] T. Nikšić, D. Vretenar, P. Ring, «Relativistic nuclear energy density functionals: Mean–field and beyond», *Prog. Part. Nucl. Phys.* **66**, 519 (2011).
- [20] T. Gonzalez-Llarena, J.L. Egido, G.A. Lalazissis, P. Ring, «Relativistic Hartree–Bogoliubov calculations with finite range pairing forces», *Phys. Lett. B* **379**, 13 (1996).
- [21] T. Nikšić, N. Paar, D. Vretenar, P. Ring, «DIRHB — A relativistic self-consistent mean-field framework for atomic nuclei», *Comput. Phys. Commun.* **185**, 1808 (2014).

- [22] Y. Tian, Z.-y. Ma, P. Ring, «Separable pairing force for relativistic quasiparticle random-phase approximation», *Phys. Rev. C* **79**, 064301 (2009).
- [23] N. Dubray, H. Goutte, J.-P. Delaroche, «Structure properties of ^{226}Th and $^{256,258,260}\text{Fm}$ fission fragments: Mean-field analysis with the Gogny force», *Phys. Rev. C* **77**, 014310 (2008).
- [24] P. Möller, A.J. Sierk, T. Ichikawa, H. Sagawa, «Nuclear ground-state masses and deformations: Frdm(2012)», *At. Data Nucl. Data Tables* **109–110**, 1 (2016).
- [25] K. Blaum, «High-accuracy mass spectrometry with stored ions», *Phys. Rep.* **425**, 1 (2006).
- [26] D. Lunney, J.M. Pearson, C. Thibault, «Recent trends in the determination of nuclear masses», *Rev. Mod. Phys.* **75**, 1021 (2003).
- [27] X.W. Xia *et al.*, «The limits of the nuclear landscape explored by the relativistic continuum Hartree–Bogoliubov theory», *At. Data Nucl. Data Tables* **121–122**, 1 (2018).
- [28] S. Raman, C.W. Nestor, P. Tikkanen, «Transition probability from the ground to the first-excited 2^+ state of even–even nuclides», *At. Data Nucl. Data Tables* **78**, 1 (2001).
- [29] M. Wang *et al.*, «The AME2016 atomic mass evaluation (II). Tables, graphs and references», *Chinese Phys. C* **41**, 030003 (2017).
- [30] A. Bohr, B.R. Mottelson, «Nuclear Deformations. Vol. II Nuclear Structure», Addison-Wesley/W.A. Benjamin, Inc., Reading, MA 1975.
- [31] I. Angeli, K.P. Marinova, «Table of experimental nuclear ground state charge radii: An update», *At. Data Nucl. Data Tables* **99**, 69 (2013).